Bioelectrochemistry 135 (2020) 107544

Contents lists available at ScienceDirect

Bioelectrochemistry

journal homepage: www.elsevier.com/locate/bioelechem

Irreversible electroporation is a thermally mediated ablation modality for pulses on the order of one microsecond

Christopher C. Fesmire, Ross A. Petrella, Jacob D. Kaufman, Nomi Topasna, Michael B. Sano *

UNC/NCSU Joint Department of Biomedical Engineering, United States

ARTICLE INFO

Article history:
Received 9 January 2020
Received in revised form 29 April 2020
Accepted 29 April 2020
Available online 5 May 2020

Keywords:
Electro-thermal therapy
High frequency irreversible electroporation
Thermally mediated electroporation
Algorithmically controlled electroporation

ABSTRACT

Irreversible electroporation (IRE) is generally considered to be a non-thermal ablation modality. This study was designed to examine the relative effect of temperature on IRE ablation sizes for equivalent dose treatments with constitutive pulses between 1 and 100 μs. 3D *in-vitro* brain tumor models maintained at 10 °C, 20 °C, 30 °C, or 37 °C were exposed to 500 V treatments using a temperature control algorithm to limit temperature increases to 5 °C. Treatments consisted of integrated energized times (doses) of 0.01 or 0.1 s. Pulse width, electrical dose, and initial temperature were all found to significantly affect the size of ablations and the resulting lethal electric field strength. The smallest ablations were created at 10 °C and E_{Lethal} were calculated to be 1729, 1359, 929, 777, 483 V/cm for 0.01 s treatments with 1, 2, 4, 8, and 100 μs pulses, respectively. At 37 °C these values decreased to 773, 614, 507, 462, and 394 V/cm, respectively. Increasing the dose from 0.01 to 0.1 s at 37 °C resulted in statistically significant decreases ($p < 0.001$) in E_{Lethal} for all treatments except for the 100 μs group. This study found that IRE is a thermally mediated, dose-dependent ablation modality for pulses on the order of one microsecond. Tissue temperatures are not accounted for when determining ablative boundaries in treatment planning algorithms. This work demonstrates that data generated at room temperature may not be predictive of ablation volumes *in-vivo* and that local temperatures should be accounted for in treatment planning.

1. Introduction

Pulsed electric fields which induce irreversible electroporation or cytotoxic phospholipid bilayer reorientation can be utilized for tumor ablation and have been demonstrated to be effective in murine models [1], canine brain tumor models [2–4], as well as in human clinical trials of liver [5], pancreatic [6], and prostate cancer [7]. Irreversible electroporation treatment is available clinically via the NanoKnife System (NK-IRE) which delivers a series of 50–100 μs electrical pulses with amplitudes between 500 and 3000 V directly to tumors via two or more needle electrodes [8]. Since its inception as a cancer therapy [9], NK-IRE has been considered a non-thermal ablation modality [10–13] due to a presumed independence of therapeutic outcomes from local tissue temperatures. Tissue heating due to resistive losses (Joule heating) is widely recognized as an effect of energy delivery [14], but is generally disregarded as an effector of ablation sizes [11,15]. It is therefore not widely accounted for in treatment planning, routinely measured clinically, nor included in active feedback during clinical use.

However, temperature changes have an effect on cell membrane fluidity and electro-permeability following exposure to 100 μs pulses [16], supplemental use of laser heating in conjunction with electrical pulse delivery has been shown to increase ablation volumes in small animals [17], and temperature changes are associated with changes in viability following exposure to nanosecond pulsed electric fields [18]. These observations indicate that local temperatures may play a role in affecting biological outcomes for certain waveforms in the nano- to microsecond pulse-duration space. Unlike other ablation technologies such as radio frequency ablation, microwave ablation or cryoablation which exert biological effects on the basis of two independent variables (temperature and time) [19], pulsed electric field effects have been harder to characterize due to their responsiveness to a combination of independent variables including pulse shape [20–22], amplitude [23], duration [24], number [25], and repetition frequency [26].

In this study, the impact of local temperatures on ablation size was investigated for pulsed electric field treatments with constitutive pulses between 1 and 100 μs. An active temperature feedback process (algorithmically controlled electroporation, ACE) [27] was integrated into the pulse delivery protocol to regulate Joule heating and mitigate temperature changes as confounding variables. Experiments were conducted on cells grown in a 3D tumor plat-

* Corresponding author.
E-mail address: mikesano@med.unc.edu (M.B. Sano).

https://doi.org/10.1016/j.bioelechem.2020.107544
1567-5394/

form with baseline temperatures of 10 °C, 20 °C, 30 °C and 37 °C. The 3D tumors were exposed to treatments at 500 V with integrated energized times (IET), a measure of dose independent of pulse width [26,28–30], between 0.01 and 0.1 s.

It was found that treatments containing constitutive pulse durations of 1, 2, 4, and 8 μs are significantly more sensitive to both local temperature and total dose than treatments with 100 μs pulse durations. At physiological temperatures, increasing the treatment dose from 0.01 to 0.1 s resulted in 39% and 7% increases in ablation diameter for treatments consisting of 1 μs and 100 μs pulses, respectively. When treatment dose was fixed to 0.1 s, increasing the baseline temperature from 20 °C to 37 °C resulted in ablation diameter increases of 66% and 4% for treatments consisting of 1 μs and 100 μs pulses, respectively. Combined, elevated temperature (20–37 °C) and dose (0.01–0.1 s) resulted in ablation diameter increases of 165%, 128%, 48%, 46%, and 34% for treatments consisting for 1 μs, 2 μs, 4 μs, 8 μs, and 100 μs waveforms, respectively. These results confirm that irreversible electroporation is a thermally mediated dose dependent ablation modality for treatments with pulses on the order of 1 μs. Using these results it is conceivable that *in vivo* treatment protocols employing microsecond electrical pulses could achieve larger ablation volumes than originally anticipated given the proper combination of dose, voltage, and treatment temperature.

2. Methods

2.1. Cell culture and treatment imaging

Human glioblastoma cells (U118, ATCC, Manassas, VA) were used due to interest in the use of electroporation in the treatment of brain tumors [31–33]. Cells were cultured following the supplier's recommended protocol in DMEM (11965118, Gibco, Gaithersburg, MD), supplemented with 2% V/V Penicillin-Streptomycin solution (15070063, Gibco, Gaithersburg, MD) and 10% V/V Fetal Bovine Serum (A3160601, Gibco, Gaithersburg, MD). Once reaching 80% confluence, the cells were harvested via trypsinization (25200056, Gibco, Gaithersburg, MD). Following centrifugation the cells were suspended in fresh media at a concentration of 1×10^6 cells/mL.

A 1:1 ratio of 5% collagen (5074-35ML, Advanced BioMatrix, San Diego, CA) and the cell suspension was created on ice with careful pipetting to prevent bubble formation. Then, 0.5 mL of the mixture was rapidly pipetted randomly into the wells of a 12-well plate using a swirling motion of the pipette tip to ensure complete coverage of the well. Following overnight incubation at 37 °C, an additional 0.5 mL of media was added. Following established protocols [26,27,30], 0.4 mL was removed immediately prior to experiments to provide a consistent load impedance and limit joule heating [27]. An additional 0.4 mL of fresh media was added to the hydrogels following treatment and samples were incubated at 37 °C for 24 h before imaging. To enable visualization of the ablation zones, live/dead staining was accomplished following a standard 30 minute incubation protocol with 2 μL of 4 μM Calcein AM (C3100MP, Invitrogen, Carlsbad, CA) and 50 μL of 100 mg/mL propidium iodide (0219545825, MP Biomedicals, Santa Ana, CA) [34]. Following staining, the samples were washed twice with 500 μL of PBS to reduce background fluorescence with care not to detach the samples from the well plates.

Imaging was accomplished via a Leica DMi8 microscope with a 4.2 megapixel digital camera (DFC9000GT, Leica Inc., Wetzlar, Germany). Micrographs of the entire well were captured at 2.5× magnification, images were stitched together using the microscope's software (LASX, Leica Inc. Wetzlar, Germany) and, cross sectional diameters of the ablations were measured. Four measurements were acquired for each ablation, one each in the horizontal and vertical directions, and two additional measurements in opposing diagonal directions. The margin of the ablation zone measurements was defined as the sub-millimeter transition from live (green) to dead cells (red) in the images. Each experimental parameter was evaluated three times (N = 3) yielding 12 measurements for each parameter. Each measurement value was then correlated to a finite element model which solved for the time and temperature dependent electric field within a domain representing the 3D tumor model, electrodes, and well plate. The electric field value that corresponded to the ablation diameter was identified as the lethal threshold for the respective experimental measurement. Ablation diameter and lethal threshold values were then averaged and are presented as mean ± standard deviation.

2.2. Treatment protocols

With the goal of the selecting pulse parameters which span current clinical treatment modalities and considering the safe operating parameters of the pulse generation system utilized a series of waveforms consisting of pulses with durations between 1 μs and 100 μs were evaluated. Given their clinical utility in alleviating muscle stimulation [35] an alternating polarity waveform consisting of a positive polarity pulse duration (P), a delay (D), and a negative polarity pulse duration (N) was investigated (Fig. 1a) and is presented using the notation P-D-N where durations have units of microseconds [μs]. Symmetric waveforms with pulse durations of 1 μs, 2 μs, 4 μs, 8 μs and a 1 μs delay between polarity changes (e.g. 8-1-8) were investigated to span the pulse duration space in proximity to the charging time of the cell membrane [24]. Additional experiments were conducted with monopolar 100 μs pulses (100-0-0) to replicate the pulses used in clinical reversible [36–38] and irreversible electroporation [2,39,40] treatments. All treatments were administered with pulse amplitudes of 500 V via a custom pulse generator based on an H-Bridge topology. An integrated 100MSPS data acquisition system was used to record and display the pulse waveforms in real time.

Treatments were administered through a custom coaxial ring and pin electrode configuration (Fig. 1b). The inner pin was fabricated from a 1.64 mm OD blunt stainless steel dispensing needle (75165A552, McMaster-Carr, Douglasville, GA). The outer ring was fabricated from 0.89 mm thick, 19 mm diameter 316 stainless steel tubing (89785 K259, McMaster-Carr, Douglasville, GA). A second blunt stainless steel dispensing needle was friction fit to the outer ring to provide an electrical connection. All components were held in place via a friction fit to a laser cut acrylic holder.

To remove temperature changes as an experimental variable, a temperature control algorithm was implemented to achieve a 5 °C temperature change from the initial temperature. A fiber optic temperature sensor (TS5, Micronor Inc., Camarillo, CA) was placed inside the center pin electrode (Fig. 1c). Temperatures were acquired (Fotemp, Micronor Inc., Camarillo, CA), transmitted over a USB Serial connection, and recorded at 3 Hz using a custom application which controlled the pulse generator output. This temperature value was used to determine the rate (R) at which energy was delivered:

$$R(T) = R_{max} \cdot \rho(T)[\mu s/s] \tag{1}$$

$$\rho(T) = 0.5 - 0.9375 \cdot \Gamma(\mathrm{T}) + 0.625 \cdot \Gamma(\mathrm{T})^3 - 0.1875 \cdot \Gamma(\mathrm{T})^5 \tag{2}$$

$$\Gamma(\mathrm{T}) = \frac{T - T_t}{\beta} \tag{3}$$

$$\beta = T_t \cdot 0.5 \tag{4}$$

where R_{max} is a user defined maximum energy delivery rate [μs/s], T is the most recent temperature measurement [°C], and T_t is the used

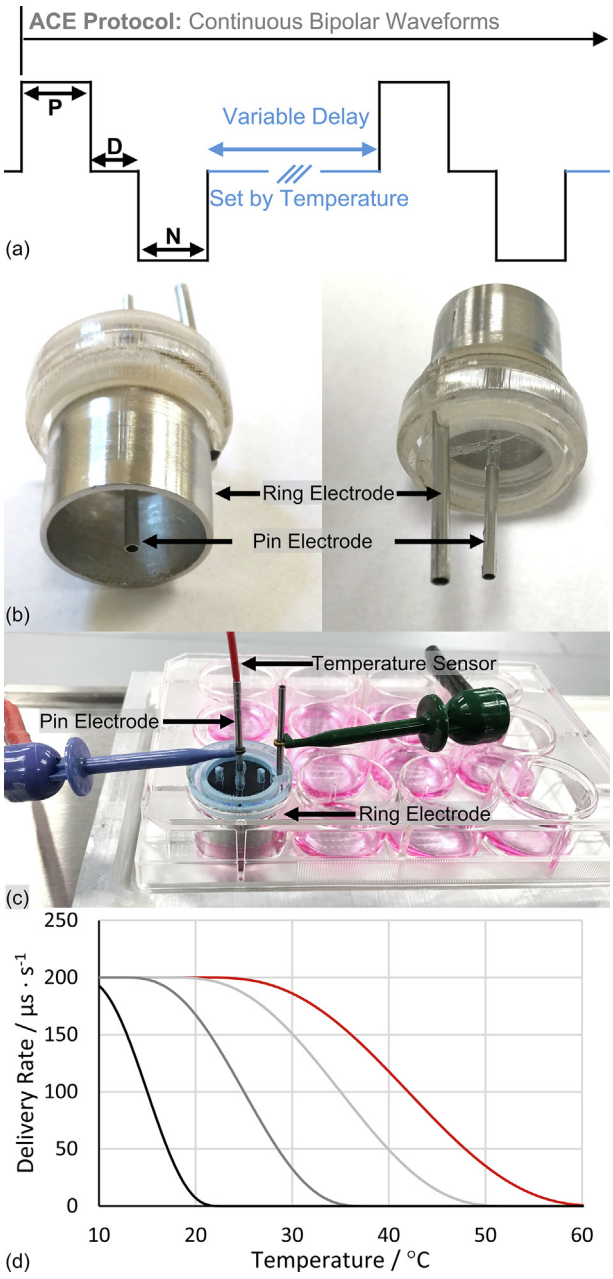

Fig. 1. (a) Schematic representing the ACE protocol consisting of bipolar electrical pulses with a variable delay between successive waveforms modified by a temperature control algorithm. The (b) Coaxial ring and pin electrode was used to deliver treatments to (c) 3D tumor models in a 12 well plate placed on top of a thermoelectric heater to maintain a specific treatment starting temperature. (d) The energy delivery rate was dynamically adjusted based on real time temperature readings to achieve a 5 °C increase in temperature to either 15 °C (black), 25 °C (dark grey), 35 °C (light grey), or 42 °C (red) independent of the treatment dose or constitutive pulse width. (For interpretation of the references to colour in this figure legend, the reader is referred to the web version of this article.)

defined target temperature [°C] (Fig. 1d). Temperature overshoot was not common in this study, but was accounted for programmatically by decreasing T_t to decelerate the pulse delivery rate.

2.3. Integrated energized time

Treatment waveforms were repeated to deliver a specified electrical dose with an integrated energized time (IET) calculated as:

$$IET = \sum_{0}^{N}(\tau_p + \tau_n)[s] \quad (5)$$

where τ_p is the positive pulse duration [µs], τ_n is the negative pulse duration [µs], and N is the total number of waveforms delivered. The primary function of the temperature control algorithm was to determine the delay (δ) between sequential waveforms required to achieve the target energy delivery rate (R) calculated as:

$$\delta = \frac{\tau_p + \tau_n}{R}[s] \quad (6)$$

Integrated times of 0.01 s and 0.1 s were investigated based on similarity to clinical protocols [3] (0.01 s) and *in vitro* results [26] which indicate diminishing returns for longer treatments (0.1 s)

Experiments were conducted with initial temperatures of 10 °C, 20 °C (room temperature), 30 °C, and 37 °C (physiological temperature). Prior to treatment, the 12 well plates were placed on a benchtop Peltier heating/cooling system (AHP-301CPV, Thermoelectric Cooling America Corporation, Chicago, IL) using a custom machined aluminum plate to aid in thermal transfer through direct mechanical contact (Fig. 1c). A thin layer of ethanol was administered between the aluminum and well plate to eliminate any air pockets and ensure efficient thermal transfer. The sample temperature was then allowed to settle to the specified treatment temperature before initiating treatment.

2.4. Finite element analysis

The electric field within the coaxial electrode is known to be spatially non-uniform [26,29] and to change over time in response to temperature dependent changes in media conductivity [41]. As such, the lethal electric field threshold (E_{Lethal}) or the minimum electric field necessary to cause cell death can be numerically determined using a finite element analysis simulation of the electric field within the electrode. The *Electric Currents* module, *Heat Transfer in Solids*, and *Electromagnetic Heating* modules in COMSOL Multiphysics (V5.3, COMSOL Inc., Palo Alto, CA) were used to compute the electric field distribution in a 2D axisymmetric model via the equations:

$$\nabla \cdot J = 0 \quad (7)$$

$$J = \sigma E \quad (8)$$

$$E = -\nabla V \quad (9)$$

where J is the local current density, E is the electric field, and V is the voltage. Dielectric charging of the media was considered to be instantaneous due to the high conductivity and relative permittivity of cell culture media.

Geometries representing a single 12-well (Fig. 2a) were created based on caliper measurements with separate domains representing the experimental electrodes, plastic well, and the cell culture media. A 500 V boundary condition was applied to the top most surface of the center pin electrode to replicate the location of the experimental gripper electrode and the top boundary of the ring electrode was set to ground:

$$V = 0[V] \quad (10)$$

The remaining external domain boundaries were set as electrical insulation:

$$n \cdot J = 0 \quad (11)$$

The electrical conductivity (σ) was set to 4.032×10^6 S/m for domains representing stainless steel components and to 1×10^{-11} S/m for domains representing plastic components. To account for temperature dependent changes within the 3D tumors, the media conductivity (σ_m) was modeled as:

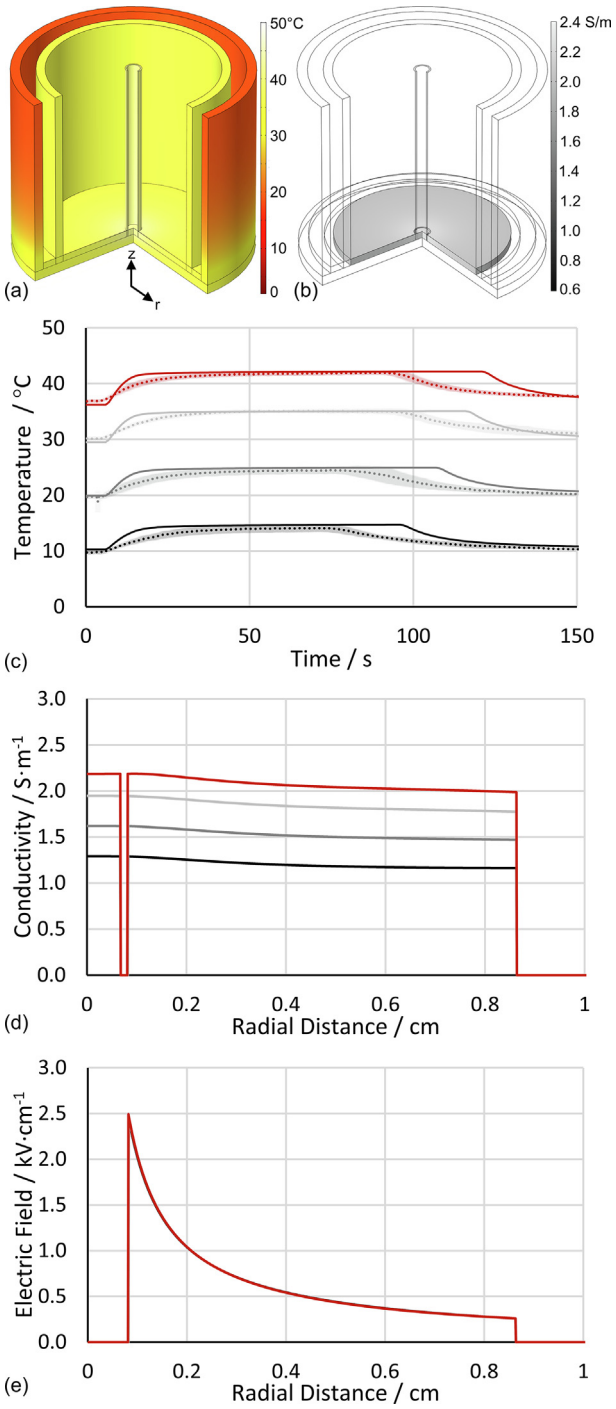

Fig. 2. Results of finite element simulations showing the (a) temperature distribution and (b) electrical conductivity distribution for 500 V 0.01 s simulations with a 37 °C initial temperature and a 42 °C temperature set point at the end of the treatment (t = 116 s). (c) Temperature profiles for treatments with 10 °C (black), 20 °C (dark grey), 30 °C (light grey), or 37 °C (red) starting temperatures at the center of the pin electrode. Solid lines represent simulated temperature profiles while dotted lines represent experimentally measured values. The shaded regions represent one standard deviation from the mean for experimentally measured values. Data was generated from a minimum of six (N = 6) representative temperature profiles selected across all waveforms. The (d) conductivity profiles and at the end of each treatment (10 °C: 92 s, 20 °C: 103, 30 °C: 112 s, 37 °C, 116 s) and (e) the radial electric field distribution. Data for each conductivity and electric field plot was derived from the bottom, center, and top of the 3D tumor geometry and is presented as the mean value. Shaded regions, representing one standard deviation from the mean, were plotted for the measured conductivity values and simulated electric field values but were not sufficiently large enough to be visible. (For interpretation of the references to colour in this figure legend, the reader is referred to the web version of this article.)

$$\sigma_m(T_L) = \alpha + \beta \cdot T_L \left[\frac{S}{m}\right] \tag{12}$$

where α was 0.6506 S/m and β was 0.0284 S/(m·°C) [41] and T_L was the local temperature in degrees Celsius. Due to the relatively low concentration of cells within the collagen matrix, it was assumed that conductivity changes due to electroporation of the cells were negligible [42]. Time dependent heating due to resistive losses were calculated via the equations:

$$\nabla \cdot (-k\nabla T) = Q_h \tag{13}$$

$$Q_h = R(T)J \cdot E \tag{14}$$

where k was the thermal conductivity, T was the local temperature, J was the local current density, and E was the local electric field. Q_h was the electromagnetic Joule heating associated with energy delivery. Q_h was scaled by a factor R(T) to account for the dynamic duty cycle associated with active temperature control. The simulations dynamically controlled the energy delivery rate to achieve temperature changes of 5 °C from the prescribed baseline temperature (10, 20, 30, or 37 °C) and Q_h was set to zero once a specified integrated energized time (IET) was achieved. To account for convective cooling, boundaries in contact with air were modeled as blackbody radiators:

$$n \cdot k\nabla T = \varepsilon(G - e_b(T)) \tag{15}$$

where G was surface irradiation and ε was the surface emissivity defined as 0.9, 0.075, and 0.97 for media, stainless steel, and plastic components, respectively. The total blackbody emissive power, e_b, was modeled as:

$$e_b(T) = n^2 \varsigma T^4 \tag{16}$$

where n was the refractive index and ς was the Stefan-Boltzmann constant (5.67×10^{-8} [W/(m^2·K^4)]).

A free tetrahedral mesh was generated in all domains using initial mesh elements with 2.36×10^{-5} cm minimum and 1.18×10^{-2} cm maximum mesh elements. The mesh was then refined via two rounds of adaptive meshing wherein the electric field magnitude (ec.normE) was used as the error indicator to ensure convergence. The final mesh consisted of 173,090 triangular elements. The simulations required approximately 15 min to solve a 200 s duration simulation for each parameter set using a ten core Intel i7-6950x processor with 64 GB of RAM.

To account for temperature changes throughout the height of the 3D tumor models, the data within the 3D tumor models was evaluated at three heights in the z-axis. 2D cut lines were generated from the center of the inner pin electrode to the edge of the outer ring electrode. The z-axis of these cut lines corresponded to the bottom, middle, and top of the 3D tumor geometry. The magnitude of the local electric fields (V/cm), temperature (°C), and electrical conductivity (S/m) along the 2D cut lines were captured at 0.001 cm intervals and exported to a spreadsheet where the values were averaged and are presented in figures as mean ± standard deviation. A lookup table was then used to correlate each measured diameter from all experimental ablations to a corresponding lethal electric field value. Results were averaged for each parameter set and are presented as mean ± standard deviation. Experimental results were statistically compared using a two sample *t*-test assuming equal variance at a significance level of α = 0.01.

3. Results

3.1. Simulated changes in local conductivity

The effect of temperature change (Fig. 2a) and temperature dependent electrical conductivity (Fig. 2b) on the electric field distribution within the 3D tumor models was investigated numerically (Supplemental Fig. 1) to determine if these factors were responsible for changes in biological response observed experimentally. These simulations also served to validate the temperature dependent ACE algorithm (Equations (1)–(6)). Simulated temperature profiles (Fig. 2c), measured at the center of the pin electrode, rapidly approached the temperature set point (5 °C greater than baseline) followed by steady state temperatures of 14.98 ± 0.11, 25.21 ± 0.09, 35.37 ± 0.09, and 42.46 ± 0.08 °C (Fig. 2c, solid lines). The simulations required a longer duration to achieve the 0.01 s dose than experimental treatments (Fig. 2c, dotted lines), likely due to the simulations reaching the target temperature more rapidly than the experimental measurements resulting in earlier throttling of the energy delivery rate. Numerically, there was spatially varying electrical conductivity distribution (Fig. 2d) at the end of energy delivery for all treatments with the highest simulated conductivity occurring at the interface between the pin electrode and the surrounding material. The profile of the conductivity distribution was similar between treatments simulated at 10, 20, 30, and 37 °C with the magnitude being dependent on the initial temperature. The simulated electric field distribution was found to vary (±5%) between the beginning and end of the treatments (Supplemental Figs. 2-3). However, at the end of each treatment (Fig. 2e), the electric field distribution was found to be independent of the initial temperature with less than 1.2% variation in the final electric field strength found within the ablation zones between treatments initiated at 10 °C and 37 °C. This final electric field distribution for each temperature set point was therefore used to calculate the corresponding experimental lethal electric field threshold.

3.2. Ablation size as a function of pulse width

Experiments conducted at 20 °C were used as a baseline representing experiments which are traditionally conducted at room temperature (Fig. 3). The treatments resulted in circular zones of dead cells, which were stained red by propidium iodide (Fig. 3-a-b), surrounded by live cells, which were enzymatically metabolizing Calcein AM into its green fluorescent components. A smaller, circular region of live cells were observed in the center of the ablations corresponding to the region inside of the center pin electrode where there is no electric field, and where temperature increases due to Joule heating were at a theoretical maximum. For treatments with IET of 0.01 s it was found that ablation size increased as a function of pulse width. The smallest ablations, measuring 2.9 ± 0.7 mm were found for treatments with 1 μs pulse durations (Fig. 3a) while the largest ablations, measuring 9.0 ± 0.3 mm, were found for treatments with 100 μs pulse durations (Fig. 3b). Between these pulse lengths, ablation size was found to sequentially increase with pulse length (Fig. 3c) with ablations measuring 3.9 ± 0.6, 6.2 ± 0.5, and 7.3 ± 0.5 mm for treatments with 2, 4, and 8 μs constitutive pulse durations.

The lethal electric field thresholds for these treatments (500 V, 0.01 s IET, 20 °C) were similarly found to be a function of constitutive pulse width (Fig. 3d). Lethal thresholds of 1497 ± 294, 1088 ± 153, 693 ± 49, 591 ± 35, and 485 ± 14 V/cm were found for 1, 2, 4, 8, and 100 μs pulse width treatments.

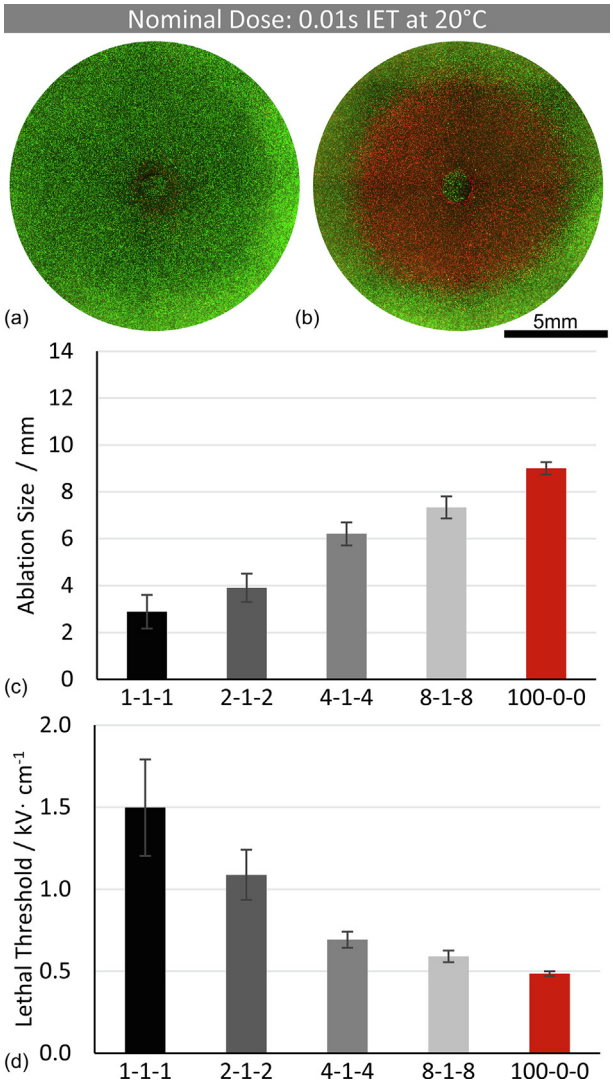

Fig. 3. Ablation size is a function of pulse duration. Representative ablations created by the (a) 1-1-1 and (b) 100-0-0 500 V 0.01 s IET treatments administered at 20 °C (room temperature) showing live (green) and dead (red) cells. (c) Ablation sizes and (d) lethal thresholds for 500V, 0.01s IET treatments with 1-1-1, 2-1-2, 4-1-4, 8-1-8, and 100-0-0 waveforms administered at 20 °C. (For interpretation of the references to colour in this figure legend, the reader is referred to the web version of this article.)

3.3. Ablation size as a function of temperature

For the 1-1-1 treatments at 10 °C, ablations measuring 2.4 ± 0.2 mm were observed (Fig. 4a). The size of the ablation zone sequentially increased for treatments administered at 20 °C (2.9 ± 0.7 mm, Fig. 4b), 30 °C (4.0 ± 1.0 mm, Fig. 4c), and 37 °C (5.5 ± 0.3 mm, Fig. 4d). A similar trend was found for the 2-1-2, 4-1-4, and 8-1-8 treatment waveforms with the smallest ablations occurring at 10 °C and sequentially larger ablations found for treatments at 20 °C, 30 °C, and 37 °C (Fig. 4e). The smallest variation in ablation size was found for the 100-0-0 waveform treatments. For this waveform, the 10, 20, and 30 °C treatments were not found to be statistically significantly different ($p > 0.072$). However, the 37 °C 100-0-0 ablation was found to be significantly larger than each of the three lower temperatures ($p < 0.001$).

The smallest lethal electric field thresholds were found for the treatments with baseline temperatures of 37 °C and were calculated as 773 ± 52, 614 ± 26, 507 ± 23, 462 ± 8, and 394 ± 37 V/cm for the 1-1-1, 2-1-2, 4-1-4, 8-1-8, and 100-0-0 waveforms,

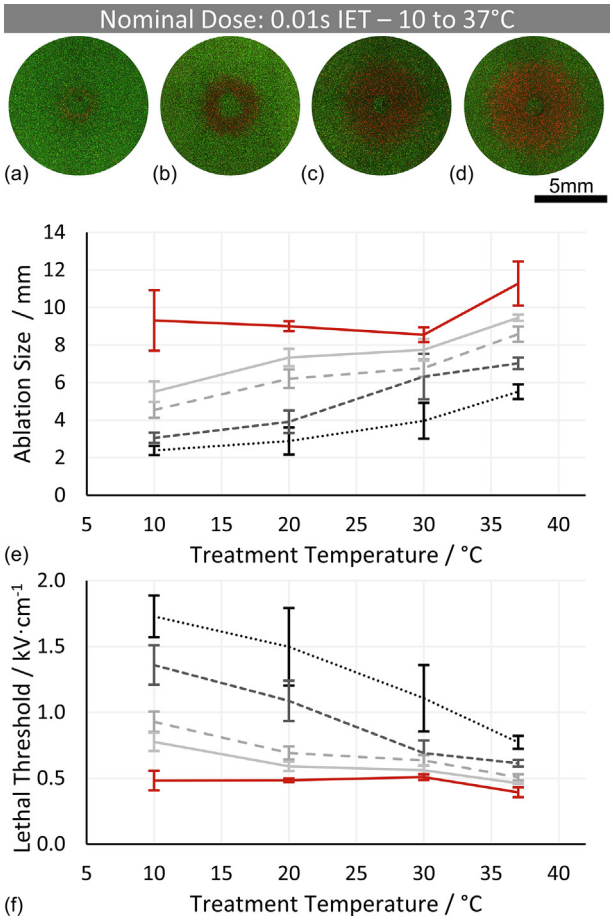

Fig. 4. Ablation sizes are a function of initial treatment temperature. The ablations created by 500 V, 0.01 s IET, 1-1-1 treatments with starting temperatures of (a) 10, (b) 20, (c) 30, and (d) 37 °C with live cells stained green and dead cells stained red. (e) Ablation sizes and (f) lethal thresholds for 500 V, 0.01 s IET as a function of starting temperature for 1-1-1 (black dots), 2-1-2 (black dashes), 4-1-4 (grey dashes), 8-1-8 (grey solid), and 100-0-0(red) waveforms. (For interpretation of the references to colour in this figure legend, the reader is referred to the web version of this article.)

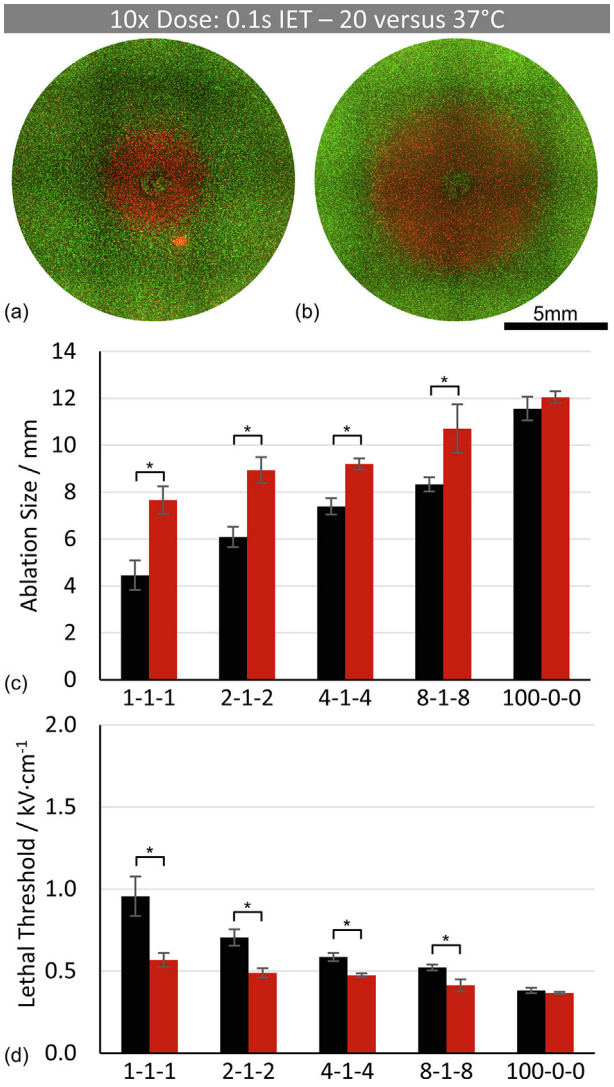

Fig. 5. Outcomes from treatments with large 0.1 s IET doses are temperature dependent. The ablations created by 500 V, 0.1 s IET, 1-1-1 treatments with starting temperatures of (a) 20 °C and (b) 37 °C. Live cells are stained green and dead cells are stained red. (c) Ablation sizes and (d) lethal thresholds for 500 V, 0.1 s IET treatments with 1-1-1, 2-1-2, 4-1-4, 8-1-8, and 100-0-0 waveforms and starting temperatures of 20 °C (black) or 37 °C (red). * represents values which were found to be statistically significantly different ($p < 0.001$). (For interpretation of the references to colour in this figure legend, the reader is referred to the web version of this article.)

respectively. A full accounting of ablation sizes and lethal electric field thresholds can be found in Supplemental Table 1.

3.4. Ablation size as a function of integrated energized time

A similar temperature dependent response was observed for treatments where the delivered dose was increased by a factor of 10 (from 0.01 to 0.1 s IET). The smallest ablations in this treatment group (500 V, 0.1 s IET) were found for protocols utilizing the 1-1-1 waveform with an initial temperature of 20 °C (4.5 ± 0.6 mm, Fig. 5a). Increasing the initial temperature to 37 °C (Fig. 5b) resulted in a significant ($p < 0.0001$) increase in ablation size to 7.7 ± 0.6 mm (Fig. 5b-c). This yielded a significant ($p < 0.0001$) decrease in lethal threshold from 957 ± 120 V/cm to 568 ± 44 V/cm (Fig. 5d). Similar statistically significant ($p < 0.0001$) increases in ablation diameter (Fig. 5c) and decreases in lethal threshold (Fig. 5d) were found for the 2-1-2, 4-1-4, and 8-1-8 waveform 0.1 s IET treatments when the initial temperature was increased from 20 °C to 37 °C. However, significant differences in ablation size ($p = 0.03$) and lethal thresholds ($p = 0.44$) were not found for the 100-0-0 waveforms between the 20 °C and 37 °C treatments. A full accounting of the ablation diameters and lethal thresholds for treatments with IETs of 0.1 s can be found in Supplemental Table 2.

3.5. Relative impact of dose and temperature

Ablations created with the 1-1-1 waveform exhibited the greatest sensitivity to changes in IET and starting temperature (Fig. 6). With IET fixed to 0.01 s, these ablations increased in diameter by 91% when the starting temperature was increased from room temperature (20 °C) to physiological temperature (37 °C). With the same waveform, an increase in diameter of 66% was observed for 10× greater dose (0.1 s IET) treatments over this temperature range (20–37 °C). In contrast, ablations created by the 100-0-0 waveform increased in diameter by 25% and 4% over this temperature range (20–37 °C) for IET of 0.01 and 0.1 s, respectively. The 2-1-2, 4-1-4, and 8-1-8 waveform treatments were also sensitive to changes in either IET or starting temperature with a general trend of decreasing effect size as pulse width increased. Comparisons of low dose (0.01 s IET) room temperature (20 °C, LD:RT) to high dose (0.1 s IET) physiological temperature (37 °C, HD:PT) treatments

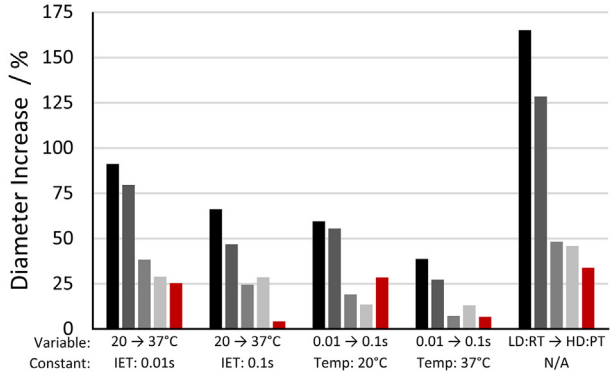

Fig. 6. Assessment of the relative impact of temperature and IET on ablation diameters. Variables represent the conditions which were changed for a given constant parameter (IET or initial temperature). LD:RT represents the low dose (0.01 s) room temperature (20 °C) treatment groups. HD:PT represents the high dose (0.1 s) physiological temperature (37 °C) treatment groups. Individual bars represent treatments administered with the 1-1-1 (black), 2-1-2 (dark grey), 4-1-4 (grey), 8-1-8 (light grey), and 100-0-0 (red) waveforms. (For interpretation of the references to colour in this figure legend, the reader is referred to the web version of this article.)

yielded increases in ablation diameters of 165%, 128%, 48%, and 46%, for 1-1-1, 2-1-2, 4-1-4, and 8-1-8 waveforms, respectively.

At physiological temperatures (37 °C), the 100-0-0 waveform displayed relatively little dependence on IET and a 10× increase from 0.01 s to 0.1 s resulted in only a 6.8% increase in ablation diameter. This waveform was similarly unaffected by treatment temperature (20 °C vs 37 °C) for treatments with IET of 0.1 s, yielding a 4.2% increase in ablation diameter. In combination, the transition from the LD:RT to HD:PT protocol resulted in an increase in ablation diameter of 34% which was smaller than any of the other waveforms investigated.

3.6. Discussion

Irreversible electroporation is generally considered to be a non-thermal ablation modality due the hypothesized independence of NK-IRE ablation sizes on local temperatures. This study contradicts that hypothesis, in particular for bipolar waveforms with pulse durations on the order of the cell membrane charging time, and demonstrates that IRE is a temperature dependent ablation modality. The extent to which these observations translate to clinical tissue ablation will need to be the focus of future work, however, preliminary studies have indicated a synergistic effect of IRE with external heating [17]. These results have significant implications related to technology development as it has been previously assumed that nano- and microsecond pulses are not capable of achieving the ablations possible with NK-IRE due to the vast majority of preclinical *in vitro* experiments being conducted at room temperature (approximately 20 °C) [23,26,29,43–45]. The baseline 20 °C treatments (Fig. 3) conducted here largely confirm the findings of prior studies that shorter pulses (1–8 μs) result in smaller ablations than 100 μs pulses with the added benefit of this study constraining tissue heating to 5 °C to further eliminate frequency and conductivity dependent Joule heating as a confounding factor. Prior studies have hypothesized that this pulse-width dependent effect was a function of cell membrane charging time [45,46] and indicated that variations in the morphologically sensitive charging time can be used to selectively target one population over another [46,47]. The results presented here follow those hypotheses to their logical conclusion that modification of the cell membrane charging time by modifying the local temperature and thus the local conductivity will have an impact on ablative outcomes. In this case, increasing temperature likely decreases the cell membrane charging time by decreasing the resistive component associated with the exponential resistive-capacitive (RC) circuit model often used to explain this phenomena.

Unfortunately, this also indicates that microsecond duration pulses may be less likely to achieve cell type specific targeting *in vivo* than at room temperature as the elevated temperatures may disproportionately reduce the charging times of one cell type over another, closing the gap which enables selectivity. It will be of interest to repeat experiments comparing lethal effects on healthy astrocytes versus brain cancer [46], and tumor initiating versus non-tumor initiating cells [47] at physiological temperatures to examine if discrimination between these cell types is still possible. Ultimately, selective targeting *in vivo* may require the utilization of sub-microsecond duration pulses [18,43,48,49] which carry their own challenges in terms of requisite electric fields, electronic equipment development, and production of electromagnetic noise in a clinical environment.

Conversely, lower temperatures may be beneficial in increasing selectivity between cell types as decreases in membrane charging rate may disproportionately affect cell types with larger membrane capacitances yielding larger charging times. Pre-cooling of tissue *in vivo* may be beneficial in reducing off-target bio-electric effects on specific cell types (e.g. nerves) in addition to the obvious effects of mitigating thermal injury. However, substantial *in vitro* and *in vivo* work will be necessary to investigate these potential effects. It is additionally unclear how changes in temperature will effect reversible or non-lethal electroporative effects *in vitro* and *in vivo*. Changes in morphology and transient electroporation effects were not explicitly investigated here and it will be of interest in future experiments to determine if cells which resided inside the area ablated at physiological temperatures exhibit a transient permeability to small molecules at hypothermic temperatures.

Interestingly, 1-1-1 and 2-1-2 waveform ablation sizes exhibited a high degree of sensitivity to both increased temperature (47–91% increase) and increased dose (27–60% increase). In combination, increases in both parameters resulted in a total change in ablation size of 165% and 128% for these waveforms, respectively (Fig. 6). This combinatorial benefit was less dramatic for the treatments with longer constitutive pulses (34–48%) indicating that for pulses approximately 1–2 μs in duration the underlying biophysics does not reach a steady state, under these experimental conditions. Increases in dose had a relatively large effect (28% increase) on the 100-0-0 ablation size at 20 °C, but only a minor effect at physiological temperatures (6%). This indicates that there is a temperature dependent dose beyond which further increases in dose have a minimal effect on ablation size. This experimental observation is confounding in light of clinical practices in which pulse delivery is continued until a specific change in tissue resistance is observed [50]. One potential explanation for the improved outcomes observed with this clinical practice, partially supported by these experiments, is that sustained pulse delivery results in hyperthermic tissue temperatures which reduce the electric field strength required to induce cytotoxic effects.

A factor in driving the transition from monopolar to bipolar waveforms for electroporation treatments was that NK-IRE ablations are relatively limited in size (compared to thermal techniques) because pulse amplitudes are constrained by the induction of intense muscle contractions. These muscle contractions must be medically managed via neuromuscular paralytics [51] and there are clinical limitations to their safety and efficacy. Preliminary *in vitro* studies indicated that pulse durations on the order of 1 μs were significantly less lethal than equivalently dosed 100 μs pulses [23,45], potentially due to bipolar cancellation effects [21,22]. This led to concerns that technologically challenging pulse amplitudes would be required to match or exceed NK-IRE ablation

volumes, potentially offsetting the reduction in muscle contractions observed with shorter pulses [35,52]. The results presented here demonstrate that lethal thresholds for 1–2 μs waveforms at physiological temperatures are within a clinically feasible range (462–614 V/cm, Fig. 4) and help to explain the disparity between thresholds derived *in vitro* at room temperature (1090–1500 V/cm, Fig. 3) and *in vivo* at physiological temperatures (522–650 V/cm [53,54]).

Early pre-clinical work has demonstrated the feasibility of 5000 V 2 μs waveforms to produce 4–5 cm ablation zones utilizing typical clinical doses (0.01–0.02 s IET) [55] and the results from this study indicate that further gains in ablation sizes with microsecond duration pulses may be possible using larger doses *in vivo*. Clinically, there are tradeoffs between the time needed to deliver higher dose treatments (0.01 versus 0.1 s IET) for marginal gains in ablation diameter versus the complexities associated with placing multiple electrodes (or electrode pairs) to achieve multiple smaller ablations with an equivalent volume. Therefore protocols requiring extreme doses (0.1 s and beyond) may not have a direct clinical benefit, but may still elucidate new aspects of the underlying biophysical phenomena.

In this study, the ability of ACE to maintain a target temperature at a single location (internal to the center electrode) was demonstrated. This enabled the examination of starting temperature on ablative outcomes due to a relatively small increase in temperature throughout the culture platform which had a negligible effect on the electric field distribution. However, it is unclear how the temperature at the ultimate ablation margin affected cell viability. Presumably *in vivo* treatments will be administered with relatively consistent temperatures (approximately 37 °C) and any positive effects provided by elevated temperature will only occur in regions affected by regional Joule heating. Future work will be necessary to demonstrate if the technology is capable of achieving a target temperature at a specified distal location (e.g. 0.5–3.0 cm from the electrode) and if this distal temperature has an impact on ablation outcomes. Due to the relatively thin cross sectional geometry of the 3D tumor models the majority of heat transfer in the system occurs vertically into the environment and heat dissipation outward from the electrode through the collagen matrix is relatively constrained. This makes investigation of multiple temperature set points at a specified distal location challenging in the present model. Future work will be necessary to either develop a more thermally insulated culture platform or to investigate these phenomena in tissue where thermal transport to the external environment is mitigated.

This study has a number of important limitations. While a broad number of experimental parameters were investigated, the effects of a single voltage were examined on a single cell line in a single collagen based cell culture platform. This material rapidly melts at temperatures above 42 °C, limiting the ability to evaluate the effects of extreme temperatures on ablation outcomes. Other *in vitro* models including media only cell suspensions can be evaluated, but direct comparisons may be challenging due to morphological changes towards spherical geometries in suspension which may affect the charging time of the cell membrane. *In vitro* models, such as the one utilized here, typically fail to recapitulate the abrupt conductivity changes due to electroporation [42] that are observed *in vivo* [56,57] and it is unclear how these changes will affect treatment outcomes *in vivo*. However, increases in tissue conductivity due to electroporation are hypothesized to positively affect cell membrane charging in a manner similar to temperature increases leading to a favorable feed forward effect. Future work will be necessary to decouple the thermal and electroporative effects on conductivity that are observed *in vivo* and it will be important to determine if processes for heating temperatures above physiological levels have a beneficial effect on ablation outcomes *in vivo* prior to using the data generated here for treatment planning purposes. Finally, utilization of the ACE algorithm to maintain a steady state temperature may increase the total treatment time especially at higher voltages (3000–5000 V) where Joule heating can become a significant factor. Future work will be necessary to develop techniques to overcome these increases if treatment times become a logistical and medical challenge in a clinical setting.

4. Conclusion

This work demonstrates that irreversible electroporation is a thermally mediated ablation modality. Temperature dependencies were highly correlated to pulse width, with the largest impact observed for treatments utilizing pulses on the order of the cell membrane charging time. Future work will be necessary to determine the *in vivo* implications of these findings, however, this preliminary work indicates that precise control over local temperatures may have a positive impact on ablation outcomes and ablation size predictability.

Declaration of Competing Interest

The authors declare the following financial interests/personal relationships which may be considered as potential competing interests: MBS has issued and pending patents related to this manuscript and receives royalties from AngioDynamics Inc. CCF and RAP have pending patents related to this manuscript and may receive royalties in the future. The remaining authors have no competing interests to declare.

Acknowledgment

This work was generously supported by the UNC/NCSU Joint Department of Biomedical Engineering.

Appendix A. Supplementary material

Supplementary data to this article can be found online at https://doi.org/10.1016/j.bioelechem.2020.107544.

References

[1] B. Al-Sakere et al., Tumor ablation with irreversible electroporation, PLoS ONE 2 (11) (2007).
[2] P.A. Garcia et al., Predictive therapeutic planning for irreversible electroporation treatment of spontaneous malignant glioma, Med. Phys. 44 (9) (Sep 2017) 4968–4980.
[3] J.H. Rossmeisl Jr et al., Safety and feasibility of the NanoKnife system for irreversible electroporation ablative treatment of canine spontaneous intracranial gliomas, J. Neurosurg. 123 (4) (2015) 1008–1025.
[4] A. G. Loganathan et al., Irreversible Electroporation for Intracranial Surgery: A Pilot Study in a Canine Model, (in English), Neuro-Oncology, Meeting Abstract vol. 11, no. 5, pp. 588-588, Oct 2009.
[5] E.I. Cohen et al., Technology of irreversible electroporation and review of its clinical data on liver cancers, Expert Rev. Med. Devices 15 (2) (Feb 2018) 99–106.
[6] R. C. Martin, 2nd et al., "Treatment of 200 locally advanced (stage III) pancreatic adenocarcinoma patients with irreversible electroporation: safety and efficacy," Ann Surg, vol. 262, no. 3, pp. 486-94; discussion 492-4, Sep 2015.
[7] M. Valerio et al., Initial assessment of safety and clinical feasibility of irreversible electroporation in the focal treatment of prostate cancer, Prostate Cancer Prostatic Dis 17 (4) (Dec 2014) 343–347.
[8] K. Thomson, "Human experience with irreversible electroporation," in Irreversible Electroporation: Springer, 2010, pp. 249-254.
[9] R.V. Davalos et al., Tissue ablation with irreversible electroporation, Ann. Biomed. Eng. 33 (2) (2005) 223–231.
[10] A. Golberg, M.L. Yarmush, Nonthermal irreversible electroporation: fundamentals, applications, and challenges, IEEE Trans. Biomed. Eng. 60 (3) (Mar 2013) 707–714.
[11] T.L. Ellis et al., Nonthermal irreversible electroporation for intracranial surgical applications: laboratory investigation, J. Neurosurg. 114 (3) (2011) 681–688.

[12] P.A. Garcia et al., Intracranial nonthermal irreversible electroporation: in vivo analysis, J. Membr. Biol. 236 (1) (Jul 2010) 127–136.
[13] C. Daniels, B. Rubinsky, Electrical field and temperature model of nonthermal irreversible electroporation in heterogeneous tissues, J. Biomech. Eng. 131 (7) (2009) 071006.
[14] M. Faroja et al., Irreversible electroporation ablation: is all the damage nonthermal?, Radiology 266 (2) (2013) 462–470.
[15] P.A. Garcia et al., Non-thermal irreversible electroporation (N-TIRE) and adjuvant fractionated radiotherapeutic multimodal therapy for intracranial malignant glioma in a canine patient, Technol. Cancer Res. Treat. 10 (1) (Feb 2011) 73–83.
[16] M. Kandušer et al., The temperature effect during pulse application on cell membrane fluidity and permeabilization, Bioelectrochemistry 74 (1) (2008) 52–57.
[17] C. M. Edelblute et al., "Controllable Moderate Heating Enhances the Therapeutic Efficacy of Irreversible Electroporation for Pancreatic Cancer," Sci Rep, vol. 7, no. 1, p. 11767, Sep 18 2017.
[18] S. Yin et al., Environmental temperature affects physiology and survival of nanosecond pulsed electric field-treated cells, J. Cell. Physiol. 233 (2) (Feb 2018) 1179–1190.
[19] C.J. Diederich, Thermal ablation and high-temperature thermal therapy: overview of technology and clinical implementation, Int. J. Hyperthermia 21 (8) (2005) 745–753.
[20] T. Kotnik et al., "Role of pulse shape in cell membrane electropermeabilization," *Biochimica et Biophysica*, Acta (BBA)-Biomembranes 1614 (2) (2003) 193–200.
[21] T. Polajžer et al., "Cancellation effect is present in high-frequency reversible and irreversible electroporation," Bioelectrochemistry, p. 107442, 2019.
[22] A.G. Pakhomov et al., Cancellation of cellular responses to nanoelectroporation by reversing the stimulus polarity, Cell. Mol. Life Sci. 71 (22) (2014) 4431–4441.
[23] M. B. Sano et al., "Bursts of Bipolar Microsecond Pulses Inhibit Tumor Growth," Sci Rep, vol. 5, p. 14999, Oct 13 2015.
[24] J.C. Weaver et al., A brief overview of electroporation pulse strength-duration space: a region where additional intracellular effects are expected, Bioelectrochemistry 87 (87) (Oct 2012) 236–243.
[25] B. Al-Sakere et al., Tumor ablation with irreversible electroporation, PLoS ONE 2 (11) (2007) e1135.
[26] M. B. Sano et al., "Burst and continuous high frequency irreversible electroporation protocols evaluated in a 3D tumor model," Phys Med Biol, vol. 63, no. 13, p. 135022, Jul 6 2018.
[27] R. A. Petrella et al., "Algorithmically Controlled Electroporation: A Technique for Closed Loop Temperature Regulated Pulsed Electric Field Cancer Ablation," IEEE Transactions on Biomedical Engineering, vol. In Press, 2020.
[28] J.D. Kaufman et al., High-Frequency Irreversible Electroporation Using 5,000-V Waveforms to Create Reproducible 2- and 4-cm Ablation Zones - A Laboratory Investigation Using Mechanically Perfused Liver, J. Vasc. Interv. Radiol. (2019).
[29] M.B. Sano et al., "Optimization of a single insertion electrode array for the creation of clinically relevant ablations using high-frequency irreversible electroporation," (in English), Comput. Biol. Med. 95 (2018) 107–117.
[30] C. C. Fesmire et al., "Temperature Dependence of High Frequency Irreversible Electroporation Evaluated in a 3D Tumor Model," Ann. Biomed. Eng., vol. In Press, 2020.
[31] P. A. Garcia et al., "Nonthermal Irreversible Electroporation as a Focal Ablation Treatment for Brain Cancer," in Tumors of the Central Nervous System, Volume 12: Springer, 2014, pp. 171-182.
[32] C.B. Arena et al., Focal blood-brain-barrier disruption with high-frequency pulsed electric fields, Technology 2 (03) (2014) 206–213.
[33] P.A. Garcia et al., 7.0-T magnetic resonance imaging characterization of acute blood-brain-barrier disruption achieved with intracranial irreversible electroporation, PLoS ONE 7 (11) (2012) e50482.
[34] C.S. Szot et al., 3D in vitro bioengineered tumors based on collagen I hydrogels, Biomaterials 32 (31) (2011) 7905–7912.
[35] M.B. Sano et al., Reduction of Muscle Contractions during Irreversible Electroporation Therapy Using High Frequency Bursts of Alternating Polarity Pulses: A Laboratory Investigation in an Ex Vivo Swine Model, J. Vasc. Interv. Radiol. (2017).
[36] G. Sersa et al., Electrochemotherapy of tumors as in situ vaccination boosted by immunogene electrotransfer, Cancer Immunol. Immunother. 64 (10) (2015) 1315–1327.
[37] D. Miklavcic et al., Electrochemotherapy: technological advancements for efficient electroporation-based treatment of internal tumors, Med. Biol. Eng. Compu. 50 (12) (Dec 2012) 1213–1225.
[38] L.M. Mir et al., Standard operating procedures of the electrochemotherapy: instructions for the use of bleomycin or cisplatin administered either systemically or locally and electric pulses delivered by the Cliniporator TM by means of invasive or non-invasive electrodes, Eur. J. Cancer Suppl. 4 (11) (2006) 14–25.
[39] S. Mafeld et al., Percutaneous Irreversible Electroporation (IRE) of Hepatic Malignancy: A Bi-institutional Analysis of Safety and Outcomes, Cardiovasc. Intervent. Radiol. 42 (4) (Apr 2019) 577–583.
[40] M. Valerio et al., Nanoknife Electroporation Ablation Trial: A Prospective Development Study Investigating Focal Irreversible Electroporation for Localized Prostate Cancer, J. Urol. 197 (3 Pt 1) (Mar 2017) 647–654.
[41] A. Mazzoleni et al., Conductivity values of tissue culture medium from 20 C to 40 C, Bioelectromagnetics 7 (1) (1986) 95–99.
[42] C.B. Arena et al., A three-dimensional in vitro tumor platform for modeling therapeutic irreversible electroporation, Biophys. J. 103 (9) (2012) 2033–2042.
[43] M.B. Sano et al., Treatment of Cancer In Vitro Using Radiation and High Frequency Bursts of Sub-Microsecond Electrical Pulses, IEEE Trans. Biomed. Eng. (2017).
[44] M. B. Sano et al., "Asymmetric Waveforms Decrease Lethal Thresholds in High Frequency Irreversible Electroporation Therapies," Sci Rep, vol. 7, p. 40747, Jan 20 2017.
[45] M.B. Sano et al., In-vitro bipolar nano- and microsecond electro-pulse bursts for irreversible electroporation therapies, Bioelectrochemistry 100 (Dec 2014) 69–79.
[46] J. W. Ivey et al., "Targeted cellular ablation based on the morphology of malignant cells," Sci Rep, vol. 5, p. 17157, Nov 24 2015.
[47] A. Rolong et al., High-frequency irreversible electroporation targets resilient tumor-initiating cells in ovarian cancer, Integr Biol (Camb) 9 (12) (2017) 979–987.
[48] A.G. Pakhomov et al., "Multiple nanosecond electric pulses increase the number but not the size of long-lived nanopores in the cell membrane," *Biochimica et Biophysica*, Acta (BBA)-Biomembranes 1848 (4) (2015) 958–966.
[49] A. Silve et al., "Comparison of the effects of the repetition rate between microsecond and nanosecond pulses: Electropermeabilization-induced electro-desensitization?," *Biochimica et Biophysica Acta (BBA)-General*, Subjects 1840 (7) (2014) 2139–2151.
[50] E.M. Dunki-Jacobs et al., Evaluation of resistance as a measure of successful tumor ablation during irreversible electroporation of the pancreas, J. Am. Coll. Surg. 218 (2) (2014) 179–187.
[51] R.C. Martin et al., Intra - operative Anesthesia Management in Patients Undergoing Surgical Irreversible Electroporation of the Pancreas, Liver, Kidney, and Retroperitoneal Tumors, Anesthesiology and pain medicine 5 (3) (Jun 2015) e22786.
[52] C.B. Arena et al., High-frequency irreversible electroporation (H-FIRE) for non-thermal ablation without muscle contraction, Biomed. Eng. Online 10 (1) (2011) 102.
[53] M. R. DeWitt et al., "Simplified Non-Thermal Tissue Ablation With A Single Insertion Device Enabled By Bipolar High-Frequency Pulses," IEEE Trans Biomed Eng, Nov 18 2019.
[54] S. Dong et al., "First human trial of high-frequency irreversible electroporation therapy for prostate cancer," Technology in cancer research & treatment, vol. 17, p. 1533033818789692, 2018.
[55] J.D. Kaufman et al., High-Frequency Irreversible Electroporation Using 5,000-V Waveforms to Create Reproducible 2-and 4-cm Ablation Zones—A Laboratory Investigation Using Mechanically Perfused Liver, J. Vasc. Interv. Radiol. (2019).
[56] R.E. Neal 2nd et al., In vivo irreversible electroporation kidney ablation: experimentally correlated numerical models, IEEE Trans. Biomed. Eng. 62 (2) (Feb 2015) 561–569.
[57] R.E. Neal et al., Experimental characterization and numerical modeling of tissue electrical conductivity during pulsed electric fields for irreversible electroporation treatment planning, Biomed. Eng., IEEE Trans. 59 (4) (2012) 1076–1085.